Probing Active Sites in Cu$_x$Pd$_y$ Cluster Catalysts by Machine-Learning-Assisted X-ray Absorption Spectroscopy

Yang Liu,[†] Avik Halder,[†] Soenke Seifert,[†] Nicholas Marcella, Stefan Vajda,* and Anatoly I. Frenkel*

Cite This: *ACS Appl. Mater. Interfaces* 2021, 13, 53363−53374

Read Online

ACCESS | Metrics & More | Article Recommendations | Supporting Information

ABSTRACT: Size-selected clusters are important model catalysts because of their narrow size and compositional distributions, as well as enhanced activity and selectivity in many reactions. Still, their structure−activity relationships are, in general, elusive. The main reason is the difficulty in identifying and quantitatively characterizing the catalytic active site in the clusters when it is confined within subnanometric dimensions and under the continuous structural changes the clusters can undergo in reaction conditions. Using machine learning approaches for analysis of the operando X-ray absorption near-edge structure spectra, we obtained accurate speciation of the Cu$_x$Pd$_y$ cluster types during the propane oxidation reaction and the structural information about each type. As a result, we elucidated the information about active species and relative roles of Cu and Pd in the clusters.

KEYWORDS: *nanocatalysts, nanoclusters, size-selected clusters, machine learning, deep learning, XANES*
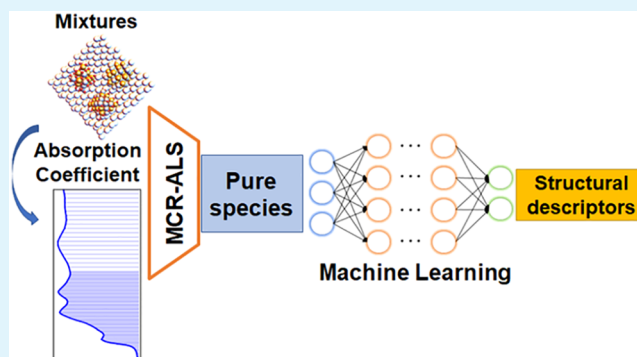
1. INTRODUCTION

Obtaining design rules for novel materials with desired performance, as a challenge toward a general goal of rational design, must rely on the knowledge of the materials' structure−activity relationships.[1−3] Many novel materials, such as nonmetal,[4−6] metal-based,[7,8] and metal oxide materials,[9,10] show unique performance at the nanoscale level. However, their structure−activity relationship is often difficult to extract by direct measurements because of the limitation of many structural probes[11] that can be applied only ex situ, and/or in restrictive environments, such as, for example, ultrahigh vacuum.[12] In addition, the understanding of structure−activity relationship requires to identify structure in working (operando) conditions, when a system, for example, a catalyst, an adsorbent, or an actuator, performs its work.[13−15]

Of those methods that are capable of determining nanoscale structure, X-ray absorption fine structure (XAFS) spectroscopy stands out. XAFS is an element-specific technique, now routinely performed under in situ/operando conditions. It provides the atomic level information including local structure details, oxidation state, and the dynamic properties of selected atomic species.[16−19] XAFS comprises two parts of the X-ray absorption coefficient measured in the energy range corresponding to the photoexcitation of the core electron in the X-ray absorbing atom: X-ray absorption near-edge structure (XANES) and extended X-ray absorption fine structure (EXAFS). The X-ray absorption fine structure in the XANES region, within 30 eV below and ~40 eV above the absorption

edge, is produced because of the transition of the core-lever electron to the unoccupied states within the absorbing and the multiple-scattering effects.[20−22] EXAFS oscillations, extending ~1000−1500 eV past the absorption edge, are explained by the interference of the outgoing and incoming photoelectron waves.[23−25] As a result, both EXAFS and XANES encode the local structural information around the absorbing atoms and enable structural investigation for a large range of materials, with a particular utility for nanomaterials.[26,27]

In this work, we focus on two topics of central interest in catalysis research. The first one is to determine the structure of the active site in multicomponent systems, the main goal of this study. The second purpose is to establish structure−activity relationship for such catalysts in reactions of practical relevance. For the latter, we have chosen the industrially relevant reactions of oxidative dehydrogenation and selective oxidation to dehydrogenate propane or perform its partial oxidation. Palladium is known as one of most active catalyst for full oxidation of hydrocarbons, including those found in automotive exhaust,[28−31] but there have also been studies reporting on the dehydrogenation propensities of Pd and its
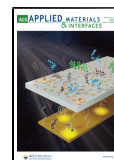
alloys.[32] At the same time, although often impeded with lower activity, copper showed a potential for use in both dehydrogenation as well as selective partial oxidation reactions.[33,34] Optimizing the catalysts for these reactions requires understanding the nature of their activity which, in turn, relies on the knowledge of active species and active sites, as the structure and oxidation state of catalytically active species may evolve in reaction conditions. We zero in on the size- and composition—selected monometallic Pd, Cu and bimetallic CuxPdy clusters, prepared with atomic precision, for two reasons. First, our hypothesis for identifying a highly active and selective catalyst is based on the exploitation of a potential symbiotic effect of a highly active Pd and a more selective Cu component. Second, these materials are chosen as part of the search of affordable replacement for the precious metals in part or in entirety, as demonstrated for example in refs.[35,36] In structural studies of size-selected clusters deposited on flat support, grazing incidence XANES (GIXANES) has been shown to contain information about the clusters' structure, oxidation states and their changes in reaction conditions.[37] GIXANES data analysis was limited, until recently, to the linear algebra methods, such as linear combination analysis with experimental standards. A recently developed machine learning-assisted interpretation of XANES spectra (ML-XANES) in monometallic Cu clusters and their oxides was shown to be useful for their structural analysis.[38−41] For bimetallic catalysts at the size scale of a few nanometers, both ML-XANES and ML-EXAFS were successfully used for their structural analysis.[42,43] In this work, and in other such systems and processes, where the catalysts undergo phase changes during the in situ XANES experiments, a combination of several structures that may coexist in reaction conditions cannot be quantitatively interpreted by the currently available ML-XANES methods.

In this article, we report on the new method of analysis of bimetallic clusters during the in situ experiment in which mixed species that comprise as few as 4−5 metal atoms coexist in time-dependent compositions: Cu_3Pd and Cu_4Pd along with their monatomic counterparts, Cu_4 and Pd_4. We demonstrate the utility of this approach for linking the composition of the clusters to their activity for propane oxidation reaction. Scheme 1 shows the procedure of resolving the structure information from the operando Cu K-edge GIXANES data. Because of the coexistence of mixed states of Cu that correspond to the coexistence of several types of clusters during the reaction, multivariate curve resolution—alternating least square (MCR-ALS) analysis was utilized as the initial step of the analysis for speciation of different types of unique metal species and to separate their spectra from the mixed signal. By performing speciation of the evolving phases using the MCR-ALS, we are able to extract the spectra about the pure phases from the mixtures during the in situ experiment. At the next step, an artificial neural network was trained, validated, tested, and finally, applied to the pure spectra of unique metal species extracted at the previous step to obtain the structure information. Finally, the information about the speciation of different states of the catalyst and their unique compositions and structures were correlated with the catalytic activity in the propane oxidation reaction.

2. EXPERIMENTAL DETAILS

2.1. Synthesis of Cu−Pd Clusters. The catalysts are prepared by soft landing of Cu_4, Cu_4Pd, Cu_3Pd, or Pd_4 clusters, which are

Scheme 1. Diagram of Machine Learning-Assisted Analysis of GI-XANES of Bimetallic Clusters
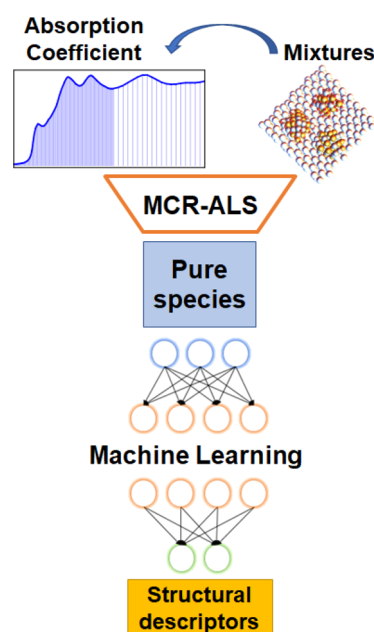
produced in a molecular beam within a high vacuum chamber, on an atomic layer-deposited alumina film[44] of three monolayer thickness (∼0.7 nm) on the top of a SiO_2/n-type (P-doped) Si wafer[44] (see Figure S1, which shows a typical mass spectrum of mono- and bimetallic clusters produced in the cluster apparatus from which a cluster of a single desired size is selected for deposition using a mass filter. On the 20 × 22 mm^2 size supports, two spots of 8 mm diameter were coated with clusters at a coverage corresponding to 10% of atomic monolayer equivalent, monitored online during deposition. Thus, all samples contained the same number of metal atoms, with a deviation smaller than 5%.[45] The clusters are landed so that the impact energy is less than 1 eV per atom, ensuring that they stay intact and do not undergo fragmentation upon landing on the substrate. More details on the cluster synthesis are given elsewhere.[45]

2.2. Operando GIXANES Experiment. The characterization of the working catalyst was performed in a home-built reactor at beamline 12-ID-C of the Advanced Photon Source at the Argonne National Laboratory.[46] This approach allows in situ X-ray monitoring of changes in the size of the clusters and follow the changes in the oxidation state of the metal, as well as to simultaneously monitor reaction product formation during temperature-programmed reaction (TPRx). The details for the reactor and the in situ experimental setup have been reported elsewhere.[46,47]

To probe the changes in the oxidation state of copper in the cluster under reaction conditions, we collected X-ray absorption near-edge spectra at a grazing incidence angle (GIXANES). To maximize the sensitivity of the experiment to the clusters lying on the surface of the support, we scattered the X-ray beam off the sample surface close to the angle of total reflection, i.e., the critical grazing incident angle of 0.3°. An additional advantage of the low angle is that a long stripe of the sample surface is illuminated, which significantly increases measured signal levels in the case of samples with very low metal coverage. GIXANES data were collected at the Cu K edge (8.9 keV) on a four-element fluorescence detector (Vortex) mounted parallel to the sample surface in order to minimize background from elastic scattering.

A complementary small-angle X-ray scattering measurement was performed at grazing incidence (GISAXS) to monitor possible agglomeration of clusters during the reaction.[46,48,49] The X-ray beam of 9.1 keV energy was scattered off the sample at the angle of incidence, 0.15° (chosen near the critical angle of 0.18° of the silicon substrate), and the two-dimensional GISAXS images were collected

on a 1024 × 1024 pixel two-dimensional Gold (modular CCD area) detector.[37] The 2D X-ray images were taken from the cluster sample at each value of temperature of the temperature ramp. The 2D scattering patterns were analyzed to obtain information about changes in the lateral and vertical dimensions of the particles, by taking cuts in the horizontal and vertical direction of the GISAXS image[37] and analyzing of these cuts with the Modeling II tool in the Irena tool suite[50] GISAXS data did not show an indication of agglomeration (see Figure S2).

The clusters were exposed to a reactant mixture composed of 3% propane and 3% oxygen seeded in He and fed into the reactor at a 18 sccm flow and under a pressure of 1.15 atm. GIXANES data were collected during the heating (25 to 550 °C) and cooling phase (550 to 25 °C) with the temperature changed in a stepwise fashion as described below.

3. MACHINE LEARNING METHOD

MCR-ALS and neural network approaches were combined in this work to provide quantitative analysis of the experimental XANES spectra. Each of the spectral components were separated from the total spectrum by the MCR-ALS and a unique Cu_x–Pd_y–O ensemble corresponding to each spectrum was tentatively proposed, as guided by the comparison with bulk standards. Finally, the neural network approach was utilized to provide quantitative structural information for each ensemble.

3.1. MCR-ALS. Because of the possible presence of mixed states of Cu electronic structure in the experimental XANES at all stages of the reaction, as evident from our previous work[40] on CO_2 methanation using CuO_x clusters, the task of XANES data analysis is 2-fold: (1) speciation and (2) structural analysis of each species. Linear combination fit (LCF) and MCR-ALS are the most commonly used techniques for studying the composition of mixtures.[41,51,52] LCF requires the use of known standards for the fitting, which is a limitation for nanomaterial studies because their XANES spectra change significantly between the bulk and nanomaterial for which there are often no standard spectra available. MCR-ALS,[53−56] on the other hand, can isolate the species and obtain their concentrations in the mixture automatically and without prior knowledge of standards. To determine the number of independent components in the MCR-ALS method, we applied principal component analysis (PCA) to the data set as the initial step.[57] Then, an iterative procedure is performed (we used the MCR-ALS toolbox[52,58]) to separate the pure species from the series of mixed spectra.

As a brief overview of the iterative procedure used by MCR-ALS, we begin with defining the input data set as the two-dimensional matrix D containing experimental XANES spectra. Then, we follow the equation $D = CS^T + E$, where C is the concentration profile, S^T is the transposed matrix containing resolved pure spectra and E is the matrix containing residuals, to express the input data set in terms of C and S^T, i.e., obtain the pure spectra and their contributions to the total spectrum at each reaction step. Two constraints are included in the fitting: (1) the non-negative values are imposed on both C and S^T, and (2) the sum of weighting factors of all pure spectra at each reaction step equals 1. At the start, the initial estimation of C and S^T are prepared by the purest variable detection method.[59,60] The fitting process is then repeated iteratively to minimize the norm $\|D - S^T\|$. More details of MCR-ALS used in this work can be found in SI Section S2).

3.2. Artificial Neural Network. Following the separation of the Cu K-edge XANES into pure components via MCR-ALS, a neural network approach could then be used to extract the structural information from the pure species. The neural network is prepared according to our previous work,[39,42] in which we described how the correlation between the XANES spectrum and the structural descriptors is built. The first nearest neighbor metal pairs of two types: Cu−Cu, Cu−Pd coordination numbers (CNs) are chosen as the structural descriptors. To train the neural network, a large training data set (containing tens to hundreds of thousands of spectra with known labels) is needed. Collecting such a data set is unrealistic from experimental perspective, and hence we used the previously developed approach[61] by which we train the neural network with synthetic data based on theoretical XANES calculated by FEFF9[62] code. To accomplish this, we first performed a theoretical benchmark by simulating the Cu K-edge XANES of standard Cu_2O and CuO. These simulations are reported in Figure S3. The optimized simulation parameters capture the major qualitative trends, and thus FEFF9 can be used for our purposes as opposed to other more detailed theoretical codes. Next, we used the Cu oxide cluster models, constructed for our previous work,[39] as the starting structures for the simulation. Pd is added to the models with ratios of Cu:Pd varied between 4:1 and 1:3, which covers the experimental clusters' composition. To incorporate the change in distances associated with Cu and Pd mixing, we approximated each particle as quasi-spherical with an average lattice constant determined by Vegard's law:

$$a_{eff} = x_{Cu}a_{Cu} + (1 - x_{Cu})a_{Pd} \tag{1}$$

where a_{eff} is the effective lattice constant, x_{Cu} is the ratio of Cu, a_{Cu} is the Cu_2O or CuO lattice constant, and a_{Pd} is the Pd_2O or PdO lattice constant, all of which are described in Table S1. The effective lattice constants were obtained to range from 2.965 to 3.052 Å for $Cu_xPd_{2−x}O$ and from 4.339 to 4.479 Å for $Cu_xPd_{1−x}O$, using eq 1. A set of theoretical site-specific XANES spectra at Cu K edge was calculated by FEFF using the optimal parameters as described in SI Section S3. To generate the site-specific training data, a set of atomistic models of $Cu_xPd_{2-x}O$ (1375 sites) and $Cu_xPd_{1−x}O$ (1287 sites) was created. The number of metal atoms are in the range of 4−83 atoms for $Cu_xPd_{2-x}O$ and 4 to 65 atoms for $Cu_xPd_{1−x}O$. All structural models are shown in Figure S4. To maximize the variability (CNs, interatomic distance, size and composition) and increase the size of our training data, a combinatorial approach was applied to the site-specific XANES. This approach has been utilized in our previous works.[39,42,61] It simulates the ensemble-averaging effect in XANES by calculating the mean of linear combination of XANES spectra and CNs, individually, for each absorbing site based on the equations:

$$\mu(E) = \sum_i \mu_i(E)/N, \quad CN_{CuCu} = \sum_i CN^i_{CuCu}/N$$

$$\text{and } CN_{CuPd} = \sum_i CN^i_{CuPd}/N$$

Using this approach, we enlarged our XANES-CN data set by randomly selecting three XANES-CNs pairs from our original site-specific data set, which is sufficiently large for training of our neural network models. To compensate for the X-ray energy shift (ΔE) between the theory and experiment, we shifted all the theoretical XANES spectra by the amount based on the difference between the experimental standards of the
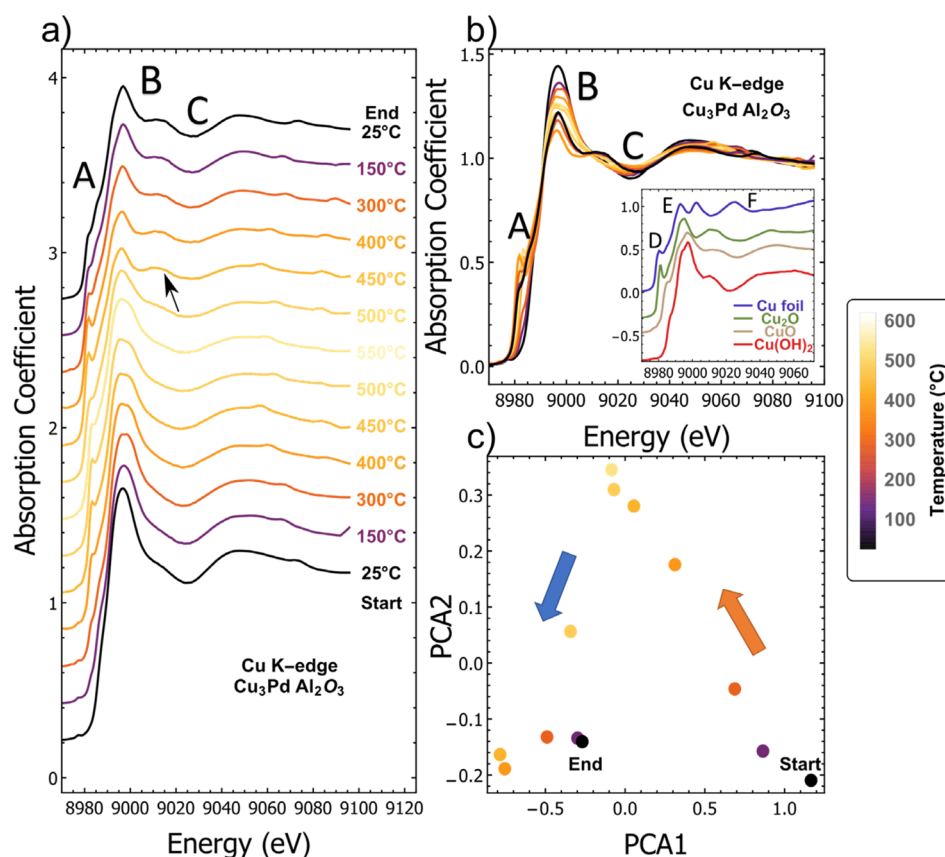
Figure 1. XANES of Cu₃Pd from 25 to 550 °C (heating cycle) and 500 to 25 °C (cooling cycle) showing temperature-resolved changes in the white line regions A, B, C (a) while shifted vertically and (b) shown in the same scale for clarity. The inset in b shows experimental XANES of Cu foil, the bulk of Cu_2O, CuO, and $Cu(OH)_2$. (c) Visualization of the data distribution from PCA analysis.

bulk and the corresponding theoretical XANES. Besides, all spectra were interpolated to the same energy scale from E_{min} = 8979.97 eV to E_{max} = 9060.21 eV. For the validation data set, we used the particle-average XANES by calculating the average XANES spectra of all the sites for each model.

Neural network training and optimization was initialized with a one-dimensional convolutional input layer based on the successful application of such a method to bimetallic nanoparticles.[42] During training, the training loss (MSE between the input and output site-specific XANES) and validation loss (MSE between the input and output particle-average XANES) are minimized. The final optimized architecture is shown in Table S2. To estimate the error in the trained neural network predictions, we followed the methodology established in ref 61. Three neural networks were trained independently to show the stability of our neural network model, and thus we report the mean prediction and error bar. More details of our theoretical simulation and neural network training are given in SI Section S3. In addition, to estimate the systematic error for the prediction on the experimental data set by the neural network, we introduced the max error to the experimental prediction process, as described in SI Section S4.

4. RESULTS AND DISCUSSION

4.1. XANES Analysis. To qualitatively interpret the evolution of the state of Cu and the structural change in the Cu_xPd_y clusters from their experimental XANES spectra, we compared their raw data with experimental data of Cu foil and

the bulk standards of Cu_2O, CuO, and $Cu(OH)_2$. The experimental XANES spectra of Cu₃Pd, Cu₄Pd, and Cu₄ are summarized in Figures 1 and 2 and Figure S5a, respectively. The data are shown for the heating cycle (25 to 550 °C) and cooling cycle (550 to 25 °C). Starting from the Cu₃Pd in Figure 1a, b, the clear change in peak intensity of the pre-edge (region A) and the shape change of main XANES part (region B and C) at different temperatures can be correlated with the changes between the references shown in Figure 1b. Specifically, at room temperature of the heating cycle, there is no visible pre-edge peak at region A but a relatively high peak intensity (>1.4) at ∼8995 eV of region B, which corresponds to the features of the bulk $Cu(OH)_2$. With the temperature increase to 400 °C, the intensity of pre-edge peak at region A gradually increases and the major peak near the edge at region B decreases, which suggests that a different structure is formed. Considering the references of Cu foil, Cu_2O, CuO and $Cu(OH)_2$ in Figure 1b, in which only Cu foil and Cu_2O have the sharp pre-edge peak at region D, we exclude the possibility of CuO and $Cu(OH)_2$. In addition, the XANES features of Cu₃Pd at around 9020 eV (region C of Figure 1b) of the heating stage (400 to 550 °C) follows the feature of the bulk Cu_2O but not Cu foil at region F of Figure 1b, in which the Cu foil has the opposite sign of the oscillation at ∼9020 eV (region F of Figure 1b). During the cooling cycle, the pre-edge feature still exists with lower peak (region A) but new feature (B) appears at ∼9014 eV in Figure 1a, as indicated by an arrow. To clarify the phase evolution, we applied PCA analysis to the Cu₃Pd. PCA reduces the dimensionality of the
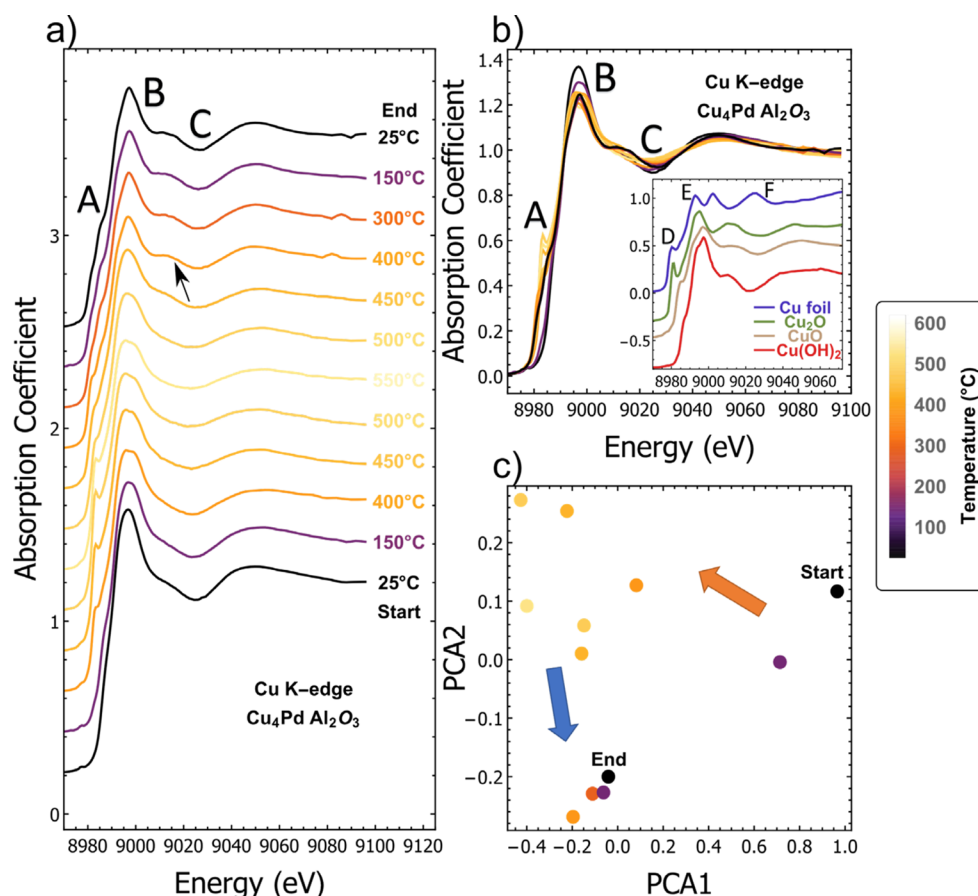
Figure 2. XANES of Cu_4Pd from 25 to 550 °C (heating cycle) and 500 to 25 °C (cooling cycle) showing temperature-resolved changes in the white line regions A, B, C (a) while shifted vertically and (b) shown in the same scale for clarity. The inset in b shows experimental XANES of Cu foil, the bulk of Cu_2O, CuO, and $Cu(OH)_2$. (c) Visualization of the data distribution from PCA analysis.
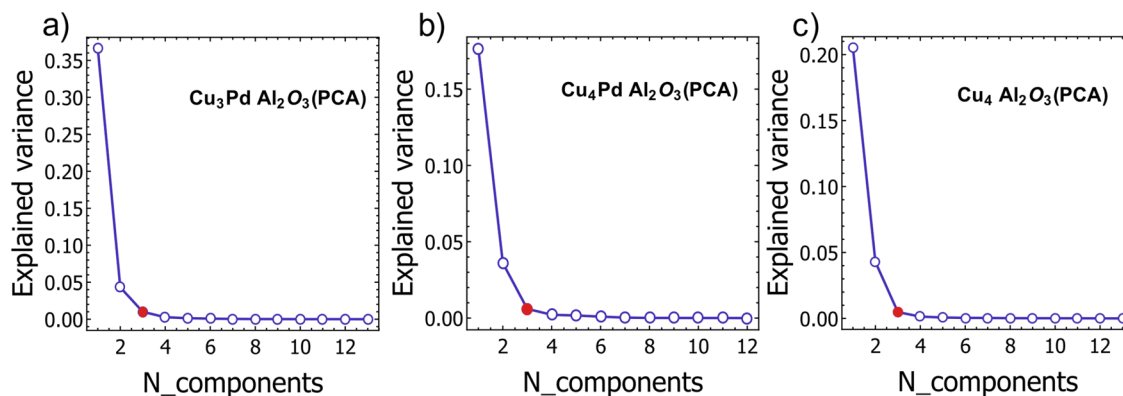

Figure 3. Correlation between the explained variance of Cu_3Pd, Cu_4Pd and Cu_4 XANES spectra and the number of principal components by PCA analysis. (a) Cu_3Pd, (b) Cu_4Pd, and (c) Cu_4. The red dots indicate that three components are sufficient for describing the entire data sets.

possible unique spectra and describes the variation caused by the original characteristics (different phases at different temperature).[63,64] Here, two-dimension representation of PCA results is displayed in Figure 1c, showing the clustering and transition in both the heating and cooling process.

Similar trends as those seen for Cu_3Pd are also observed in Cu_4Pd and Cu_4 in Figure 2 and Figure S5, where both Cu_4Pd and Cu_4 show a clear pre-edge peak (region A) at from 400 to 550 °C during the heating cycle. During the cooling cycle, the pre-edge feature exists with lower peak (region A) and new feature (B) appears at ~9014 eV in Figure 1a, as indicated by

an arrow. However, there are some differences in the cooling process, where Cu_3Pd still has a clear pre-edge peak (region A) from 500 to 400 °C but Cu_4Pd and Cu_4 exhibit a lower pre-edge feature (region A) during the cooling cycle. In summary, Cu_3Pd, Cu_4Pd, and Cu_4 show clear phase transitions during the heating and cooling cycle.

4.2. MCR-ALS Results. To identify the different phases and obtain their ratios in operando conditions at different temperatures, we carried out the MCR-ALS analysis of Cu XANES data. To obtain the number of unique spectra corresponding to the pure species present in the operando
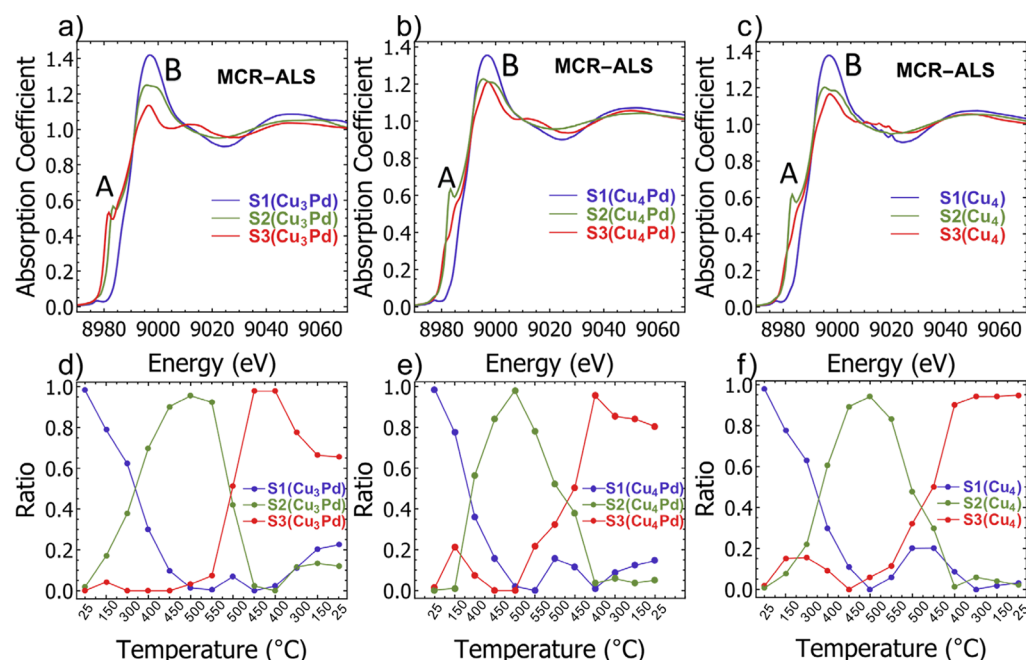
Figure 4. Results of the MCR-ALS analysis of Cu_3Pd, Cu_4Pd and Cu_4. (a−c) Resolved pure species by MCR-ALS for Cu_3Pd, Cu_4Pd, and Cu_4. (d−f) Concentration profile obtained by MCR-ALS for Cu_3Pd, Cu_4Pd, and Cu_4.
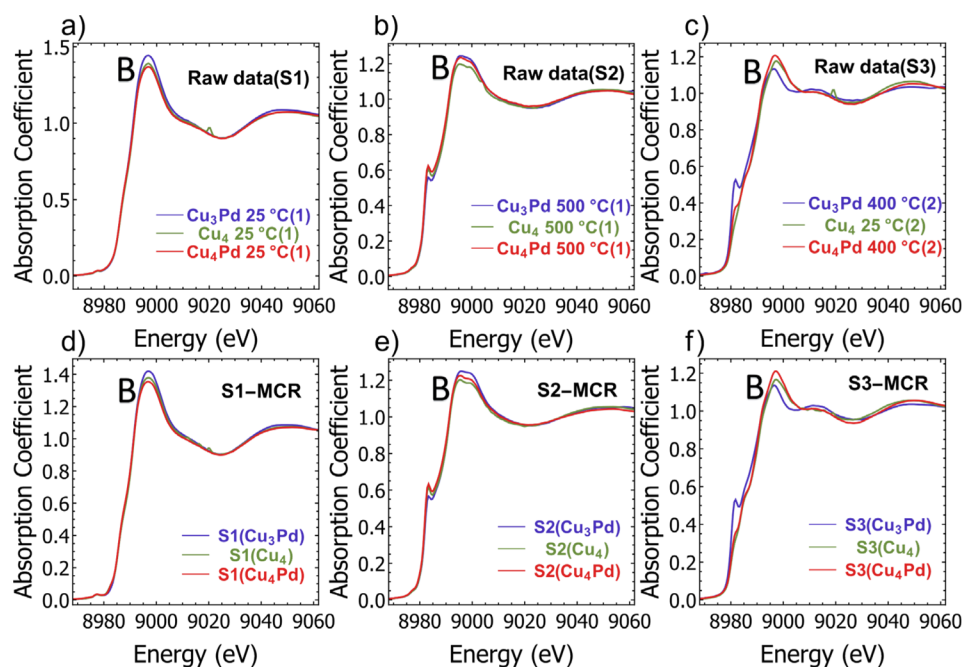

Figure 5. Comparison of MCR results with the experimental XANES which has the largest fraction of pure species from the MCR analysis. (a−c) Experimental XANES, which has the largest fraction of pure species from the MCR analysis. (d−f) Pure species from the MCR-ALS results.

experiment, PCA was applied to each data set and the explained variance (eigenvalues in PCA) is shown in Figure 3. The crossover between the initial variances, up to the third component (indicated by red dots in Figure 3), and the rest of the values, indicates that three components are sufficient to describe the entire data set for each of the three catalysts.

The MCR-ALS analysis resulted in the isolation of the spectra for each species, including their concentration profiles, for each of the catalyst. In Figure 4a−c, three separated spectra S1−S3 displayed unique pre-edge at region A and main XANES features at region B. In summary, S1 has a higher peak

intensity near the edge (region B) and no clear pre-edge peak (region A). S2 has the sharp pre-edge peak at region A and a relatively lower peak at region B. For S3 species, they have the lowest pre-edge peak (region A) and different XANES features (region B) compared to the other two phases. In Figure 4d−f, the fractions of each species at different temperatures are shown. At the start of heating cycle, the clusters show a nearly pure phase of S1. With the temperature increase, the concentration of S1 decreases and the ratio of the S2 species starts to increase. At 500 °C in the heating part, the S2 species reaches the highest ratio. Then, the fraction of S3 species starts
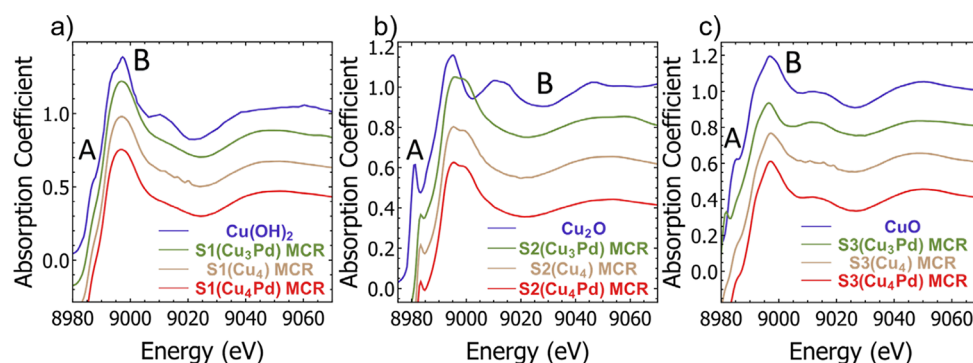
Figure 6. Comparison of MCR-ALS results and standard spectra for $Cu(OH)_2$, Cu_2O and CuO. (a) $Cu(OH)_2$ standard and S1 spectra for Cu_3Pd, Cu_4, and Cu_4Pd. (b) Cu_2O standard and S2 spectra for Cu_3Pd, Cu_4, and Cu_4Pd. (c) CuO standard and S3 spectra for Cu_3Pd, Cu_4, and Cu_4Pd.

to increase and those of the other two species (S1, S2) decrease. The concentration profile is correlated with our previous observation of the experimental data in Figures 1 and 2a and Figure S3a, where the unique features (at region A and B) are observed, respectively, at the beginning of heating, the higher temperatures (400 to 500 °C) of the heating cycle, and the lower temperatures (400 to 25 °C) of the cooling cycle.

In addition, from the concentration profile shown in Figure 4d−f, nearly pure phases are found at 25 and 500 °C of the heating cycle and 400 °C in the cooling cycle. To examine the capability of the MCR-ALS to separate the independent spectra, we compared the S1, S2, and S3 of Cu_3Pd, Cu_4Pd, and Cu_4 with the experimental data at those temperatures with the highest fraction of pure species shown in Figure 5a−c. The results show that three pure phases separated from MCR-ALS in Figure 5d-f exhibit similar features (in region B) compared to the raw data in Figure 5a−c. In addition, for each species, there is also a trend in region B correlated with different clusters (Cu_3Pd, Cu_4, and Cu_4Pd). For example, the Cu_3Pd have the highest peak intensity compared to Cu_4Pd in Figure 5a, b. However, the trend is reversed in Figure 5c. In summary, following the high temperature, the formation of different phases from our MCR-ALS analysis cause the change in average structure.

To analyze each species corresponding to S1, S2 and S3, the Cu foil, the bulk of $Cu(OH)_2$, Cu_2O and CuO are utilized as guidance for comparing with the spectra denoted as S1−S3 for each of the samples: Cu_3Pd, Cu_4 and Cu_4Pd, shown in Figure 6. For S1 species in Figure 6a, there is no pre-edge feature at region A but high peak near the edge position at region B, which matches the feature of $Cu(OH)_2$ from Figure 6a. For S2 species in Figure 6b, the feature of the sharp pre-edge peak at region A is associated with the standard of Cu_2O and Cu foil in Figure 1b region D. In addition, S2 species follows the features of Cu_2O at region B of Figure 6b but not the Cu foil because Cu foil has the opposite oscillation (region F in Figure 1b) at around 9020 eV and relatively lower peak intensity in the main XANES region (region E in Figure 1b). For S3 phase in Figure 6c, the features at pre-edge (region A) and main XANES region (region B) match the standard of CuO, hence they are assigned to CuO phase. Because of the nanoscale effect and the alloyed Pd with Cu, the peak shape in the main XANES region is expectedly different from the bulk Cu reference spectra. However, the trend of the XANES in the A, B regions (Figure 6) can be qualitatively compared with the corresponding trends in the reference Cu spectra. Besides, pre-edge features are unique and are often qualitatively similar for the bulk and

the nanoparticles. Hence, we assigned our MCR-ALS results to each type of species with the closest match of their respective features.

4.3. Neural Network Results. To extract the structural information from those pure species separated by MCR-ALS, we performed neural network-XANES analysis. The training data were constructed by the FEFF simulation described in SI Section S3. Because of the complexity of the $Cu(OH)_2$ models, only S2 and S3 species were studied; they also have more influence on the catalytic activity. To show the effect of Pd in the XANES simulation, we used different ratios of Cu:Pd from 1:3, 1:1 to 3:1 in Figure 7. The results demonstrate that
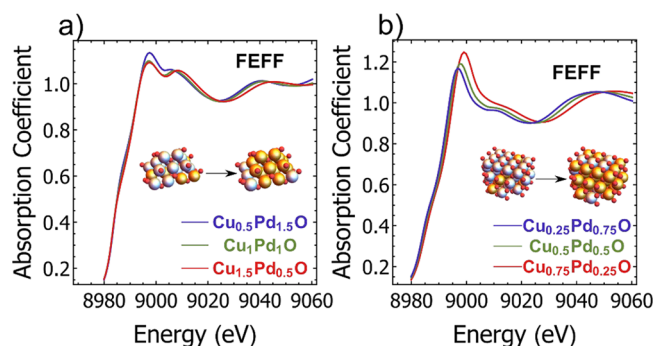

Figure 7. Compositional effect on the selected particles of (a) $Cu_xPd_{2−x}O$ with ratios of Cu:Pd ranging from 1:3 to 1:1 to 3:1 and (b) $Cu_xPd_{1−x}O$ with ratios of Cu:Pd ranging from 1:3 to 1:1 to 3:1.

XANES shifts to the lower energies with the increase in the Pd:Cu ratio and the peak intensity near the edge position exhibits the systematic trend for the selected particles, where the peak intensity near the edge position increases with the increase in the Cu ratio. The trend is also comparable with the MCR-ALS results in Figure 5. To validate our trained neural network, we fed particle-averaged XANES of $Cu_xPd_{2−x}O$ and $Cu_xPd_{1−x}O$ into our trained neural network. The theoretical models for our validation are listed in the Figure S4. The results are shown in Figure 8, for both $Cu_xPd_{2−x}O$ and $Cu_xPd_{1−x}O$ specific neural networks, where the median absolute deviation in CN prediction is very low and suggests the prediction of the median CNs is very stable. The standard deviation from the ensemble of three neural network models provided the estimation of the error as shown in Figure 8. Then, we applied our trained neural network to evaluate the Cu_3Pd, Cu_4Pd from MCR-ALS analysis and summarized the results in Table 1. For the analysis of Cu_4 clusters, we relied on
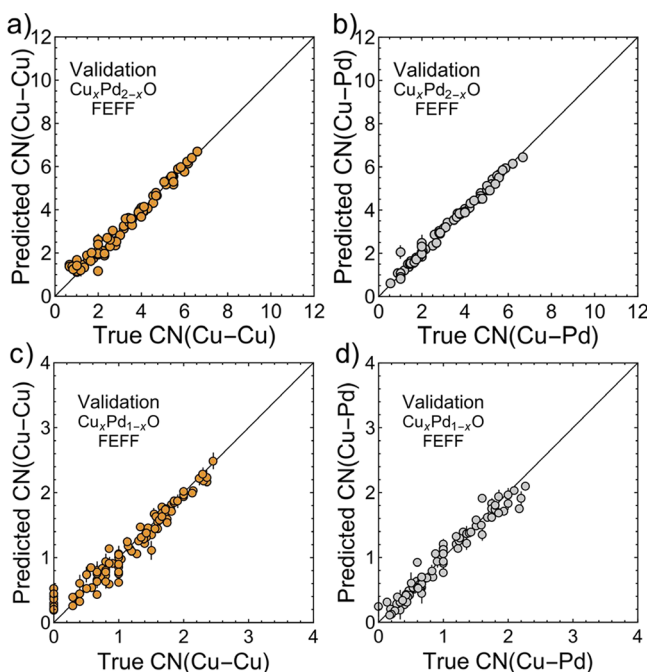
Figure 8. True values of CN(Cu−Cu), CN(Cu−Pd) vs predicted values of CN(Cu−Cu), CN(Cu−Pd) for the first shell: (a) CN(Cu−Cu), (b) CN(Cu−Pd) obtained using the $Cu_xPd_{2−x}O$ neural network model, (c) CN(Cu−Cu), (d) CN(Cu−Pd) obtained using the $Cu_xPd_{1−x}O$ neural network model.

our previously developed neural network.[39] To incorporate the systematic error from our neural network based on the validation results, we calculated the max error and added to our experimental evaluation. The detailed description of the max error is given in SI Section 4. From the results in Table 1, it is evident the CN(Cu−Cu) increases, and CN(Cu−Pd) decreases, with the increase in Cu ratio. Besides, the prediction from neural network is not consistent with forming large aggregates because the low coordination numbers of Cu−Cu and Cu−Pd correspond to cluster sizes that are consistent with our GISAXS results shown in Figure S2.

4.4. Catalytic Activity and Its Correlation with the Structure. The reactivity of clusters is investigated with a reactant gas consisting of a mixture of 3% propane and 3% of oxygen seeded in helium, fed into the reactor at a flow rate of 18 sccm and a cell pressure of 1.1 atm. The temperatures applied are 25, 50, 150, 300, 400, 450, 500, and 550 °C, with a slow heating between the individual temperature steps to ensure thermal stabilization. The reaction products are identified and their evolution with temperature followed using mass spectrometry. The reaction rates (r) obtained from mass spectra data collected during the heating phase

ramp for the clusters that underwent detailed interrogations for the evolution of their structure and oxidation state above are shown in (Figure 9) reaching up to about 1.2 molecules/second/metal atom for propylene oxide, which is significantly higher than the rates obtained by currently used techniques where propylene or a mixture of propane and propylene are used as the starting gases.[65−68] Pd_4, with a high level of combustion to CO_2 turns out to have the lowest activity as well as the lowest selectivity toward C3 products. In contrary, for the CuPd clusters with prevailing Cu content, both the reaction rate and the selectivity toward C3 products dramatically increases. The rates obtained for the studied clusters go by the following order. Propylene oxide formation: $Pd_4 \ll Cu_3Pd = Cu_4Pd$. Propylene production: $Pd_4 \ll Cu_3Pd < Cu_4Pd$. Such order can be correlated with our structural analysis by neural network-XANES analysis in Table 1 where Cu_4Pd shows a larger Cu−Cu coordination number and lower Cu−Pd coordination number. Selectivity for both propylene oxide and propylene formation are overall high and very similar for the mixed CuPd clusters in the 150−300 °C range and at higher temperatures, respectively. The performance of Cu_4 clusters (shown in ref 40) was comparable to that of Cu_4Pd.

In our studies, at elevated temperatures, both Cu_3Pd and Cu_4Pd exhibit high catalytic activity, with unique selectivity toward propylene oxide or propylene between 150 and 300 °C and 450−550 °C, respectively, which can be also explained by the onset of phase transition between 150−300 °C range by our MCR-ALS analysis (Figure 4). Combining the MCR-ALS results with the reactivity study, we conclude that it is the Cu(+) phase, which at elevated temperatures is correlated with the high catalytic activity of the Cu-containing species. The temperature mainly affects the Cu oxidation state. The theoretical study from the ref 33 provides the explanation of the unique activity of oxidized Cu during the oxidation reaction. However, on basis of the available data, it is not possible to unambiguously determine whether it is the oxidation state or the structure from refs 33 and 69 alone, that has the exclusive or dominant effect on the performance, or the combination of these two phenomena. The benefits of Cu in the studied catalysts are 2-fold: dramatically improved performance in the reaction and significant economic impact on the catalyst price due to the reduced or eliminated use of Pd in the studied and potentially other oxidative processes as well.

■ CONCLUSIONS

The structure−activity relationship was investigated for propane oxidation reactions using size-selected Cu_xPd_y clusters and studied by synchrotron-based XANES combined with the simultaneous monitoring of catalytic performance. Using a combination of MCR-ALS and neural network-based machine

Table 1. Prediction of Species S2 and S3 from MCR-ALS Results by the $Cu_xPd_{2−x}O$ (Cu_2O) and $Cu_xPd_{1−x}O$ (CuO) Neural Network Models

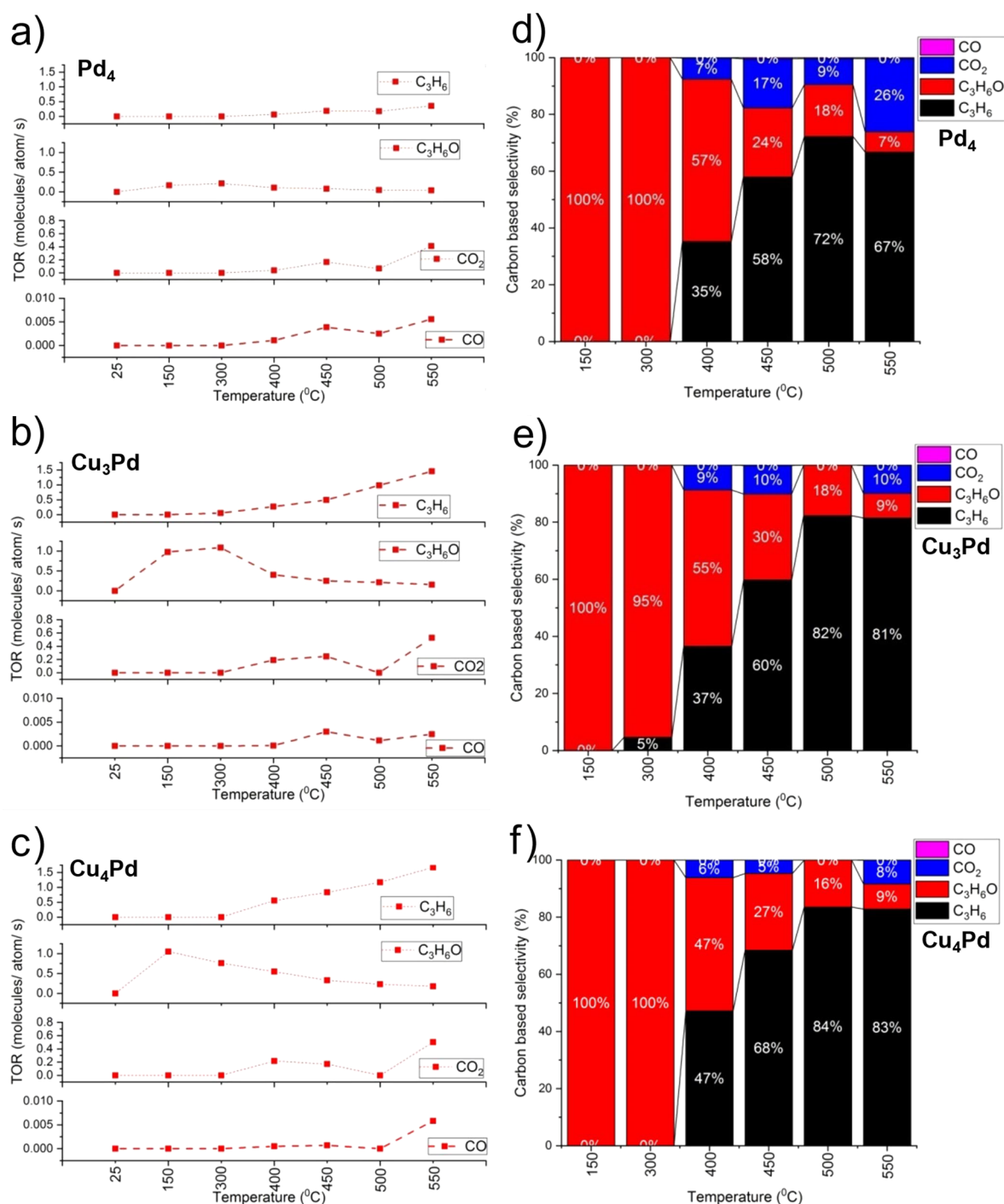| MCR-ALS	S2−Cu_3Pd	S2−Cu_4Pd	S2−Cu_4	S3−Cu_3Pd	S3−Cu_4Pd	S3−Cu_4
predicted CN(Cu−Cu)	2.3 ± 0.4	2.6 ± 0.4	3.3 ± 0.5	2.2 ± 0.3	2.4 ± 0.1	3.5 ± 0.1
predicted CN(Cu−Pd)	1.0 ± 03	0.7 ± 0.2		1.4 ± 0.3	1.3 ± 0.2	
predicted CN(Cu-M)	3.3 ± 0.5	3.3 ± 0.4	3.3 ± 0.5	3.6 ± 0.4	3.7 ± 0.2	3.5 ± 0.1

Figure 9. Rate of formation and carbon-based selectivity for reaction products during oxidative dehydrogenation of propane over alumina-supported Cu and Cu_xPd_y clusters. Rates for the major products propylene, propylene oxide, and the byproducts CO, and CO_2 are plotted for (a) Pd_4, (b) Cu_3Pd, and (c) Cu_4Pd cluster catalysts. Carbon-based selectivity for the reaction products are plotted for (d) Pd_4, (e) Cu_3Pd, and (f) Cu_4Pd cluster catalysts.

learning methods for XANES data analysis, we obtained speciation of chemical states and compositions of Cu species in Cu and CuPd clusters, along with information about their structure, and correlated these results with catalyst activity and selectivity. Cu was found to be the source of the enhancement of catalytic activity and selectivity toward C3 products. The MCR-ALS analysis also provided an explanation for the change in activity and selectivity with temperature, identifying Cu^+ species and structures with high Cu−Cu and low Cu−Pd coordination numbers as the roots of the improved catalytic

performance. This case study demonstrates the potential of the applicability of MCR-ALS and machine learning-assisted analysis of operando XANES spectra to the mechanistic understanding a broad class of ultrasmall bimetallic cluster-based catalysts.

■ ASSOCIATED CONTENT

ⓢ Supporting Information

The Supporting Information is available free of charge at https://pubs.acs.org/doi/10.1021/acsami.1c06714.

Mass spectrum of clusters; details of XANES simulation by FEFF9 for Cu_xPd_y atomic clusters and nanoparticles; MCR-ALS analysis used for the experimental XANES analysis; neural network analysis for the evaluation of the theoretical and experimental XANES (PDF)

■ AUTHOR INFORMATION

Corresponding Authors

Anatoly I. Frenkel − *Department of Materials Science and Chemical Engineering, Stony Brook University, Stony Brook, New York 11794, United States; Chemistry Division, Brookhaven National Laboratory, Upton, New York 11973, United States;* orcid.org/0000-0002-5451-1207; Email: anatoly.frenkel@stonybrook.edu

Stefan Vajda − *Materials Science Division, Argonne National Laboratory, Argonne, Illinois 60439, United States; Institute for Molecular Engineering, The University of Chicago, Chicago, Illinois 60637, United States; Department of Nanocatalysis, J. Heyrovský Institute of Physical Chemistry, Czech Academy of Sciences, Prague 8 18223, Czech Republic;* orcid.org/0000-0002-1879-2099; Email: stefan.vajda@jh-inst.cas.cz

Authors

Yang Liu − *Department of Materials Science and Chemical Engineering, Stony Brook University, Stony Brook, New York 11794, United States*

Avik Halder − *Materials Science Division, Argonne National Laboratory, Argonne, Illinois 60439, United States*

Soenke Seifert − *X-ray Science Division, Argonne National Laboratory, Argonne, Illinois 60439, United States*

Nicholas Marcella − *Department of Materials Science and Chemical Engineering, Stony Brook University, Stony Brook, New York 11794, United States;* orcid.org/0000-0002-2224-532X

Complete contact information is available at:
https://pubs.acs.org/10.1021/acsami.1c06714

Author Contributions

[†]Y.L., A.H., and S.S. contributed equally to this work.

Notes

The authors declare no competing financial interest.

■ REFERENCES

(1) Chen, Y.; Lai, Z.; Zhang, X.; Fan, Z.; He, Q.; Tan, C.; Zhang, H. Phase Engineering of Nanomaterials. *Nat. Rev. Chem.* **2020**, *4* (5), 243−256.

(2) Walsh, T. R.; Knecht, M. R. Biointerface Structural Effects on the Properties and Applications of Bioinspired Peptide-Based Nanomaterials. *Chem. Rev.* **2017**, *117* (20), 12641−12704.

(3) Bediako, D. K.; Lassalle-Kaiser, B.; Surendranath, Y.; Yano, J.; Yachandra, V. K.; Nocera, D. G. Structure-Activity Correlations in a Nickel-Borate Oxygen Evolution Catalyst. *J. Am. Chem. Soc.* **2012**, *134* (15), 6801−6809.

(4) Liu, D.; Ni, K.; Ye, J.; Xie, J.; Zhu, Y.; Song, L. Tailoring the Structure of Carbon Nanomaterials toward High-End Energy Applications. *Adv. Mater.* **2018**, *30* (48), 1802104.

(5) Zhao, Y.; Nakamura, R.; Kamiya, K.; Nakanishi, S.; Hashimoto, K. Nitrogen-Doped Carbon Nanomaterials as Non-Metal Electrocatalysts for Water Oxidation. *Nat. Commun.* **2013**, *4*, 2−8.

(6) Pahalagedara, L.; Sharma, H.; Kuo, C. H.; Dharmarathna, S.; Joshi, A.; Suib, S. L.; Mhadeshwar, A. B. Structure and Oxidation Activity Correlations for Carbon Blacks and Diesel Soot. *Energy Fuels* **2012**, *26* (11), 6757−6764.

(7) Makvandi, P.; Wang, C. yu; Zare, E. N.; Borzacchiello, A.; Niu, L. na; Tay, F. R. Metal-Based Nanomaterials in Biomedical Applications: Antimicrobial Activity and Cytotoxicity Aspects. *Adv. Funct. Mater.* **2020**, *30* (22), 1910021.

(8) Xia, Z.; Guo, S. Strain Engineering of Metal-Based Nanomaterials for Energy Electrocatalysis. *Chem. Soc. Rev.* **2019**, *48* (12), 3265−3278.

(9) Kirumakki, S. R.; Shpeizer, B. G.; Sagar, G. V.; Chary, K. V. R.; Clearfield, A. Hydrogenation of Naphthalene over NiO/SiO2-Al2O3 Catalysts: Structure-Activity Correlation. *J. Catal.* **2006**, *242* (2), 319−331.

(10) Nguyen, M. A.; Bedford, N. M.; Ren, Y.; Zahran, E. M.; Goodin, R. C.; Chagani, F. F.; Bachas, L. G.; Knecht, M. R. Direct Synthetic Control over the Size, Composition, and Photocatalytic Activity of Octahedral Copper Oxide Materials: Correlation between Surface Structure and Catalytic Functionality. *ACS Appl. Mater. Interfaces* **2015**, *7* (24), 13238−13250.

(11) Weckhuysen, B. M. Snapshots of a Working Catalyst: Possibilities and Limitations of in Situ Spectroscopy in the Field of Heterogeneous Catalysis. *Chem. Commun.* **2002**, *2* (2), 97−110.

(12) Yang, J. C.; Bharadwaj, M. D.; Zhou, G.; Tropia, L. *Microsc. Microanal.* **2001**, *7*, 486−493.

(13) Frenkel, A. I.; Cason, M. W.; Elsen, A.; Jung, U.; Small, M. W.; Nuzzo, R. G.; Vila, F. D.; Rehr, J. J.; Stach, E. A.; Yang, J. C. Critical Review: Effects of Complex Interactions on Structure and Dynamics of Supported Metal Catalysts. *J. Vac. Sci. Technol., A* **2014**, *32* (2), 020801.

(14) Tsoukalou, A.; Abdala, P. M.; Stoian, D.; Huang, X.; Willinger, M. G.; Fedorov, A.; Müller, C. R. Structural Evolution and Dynamics of an In2O3 Catalyst for CO2 Hydrogenation to Methanol: An Operando XAS-XRD and in Situ TEM Study. *J. Am. Chem. Soc.* **2019**, *141* (34), 13497−13505.

(15) Vuurman, M. A.; Wachs, I. E. In Situ Raman Spectroscopy of Alumina-Supported Metal Oxide Catalysts. *J. Phys. Chem.* **1992**, *96* (12), 5008−5016.

(16) Koningsberger, D. C.; Prins, R. *X-Ray Absorption: Principles, Applications, Techniques of EXAFS, SEXAFS, and XANES*; Wiley, 1988.

(17) Yamamoto, T.; Suzuki, A.; Nagai, Y.; Tanabe, T.; Dong, F.; Inada, Y.; Nomura, M.; Tada, M.; Iwasawa, Y. Origin and Dynamics of Oxygen Storage/Release in a Pt/Ordered CeO 2-ZrO2 Catalyst Studied by Time-Resolved XAFS Analysis. *Angew. Chem., Int. Ed.* **2007**, *46* (48), 9253−9256.

(18) Farges, F.; Lefrère, Y.; Rossano, S.; Berthereau, A.; Calas, G.; Brown, G. E. The Effect of Redox State on the Local Structural Environment of Iron in Silicate Glasses: A Combined XAFS Spectroscopy, Molecular Dynamics, and Bond Valence Study. *J. Non-Cryst. Solids* **2004**, *344* (3), 176−188.

(19) O'Day, P. A.; Rehr, J. J.; Zabinsky, S. I.; Brown, G. E. Extended X-Ray Absorption Fine Structure (EXAFS) Analysis of Disorder and Multiple-Scattering in Complex Crystalline Solids. *J. Am. Chem. Soc.* **1994**, *116* (7), 2938−2949.

(20) Rehr, J. J.; Albers, R. C.; Zabinsky, S. I. High-Order Multiple-Scattering Calculations of x-Ray-Absorption Fine Structure. *Phys. Rev. Lett.* **1992**, *69* (23), 3397−3400.

(21) Mukerjee, S.; Srinivasan, S.; Soriaga, M. P.; McBreen, J. Role of Structural and Electronic Properties of Pt and Pt Alloys on Electrocatalysis of Oxygen Reduction: An In Situ XANES and EXAFS Investigation. *J. Electrochem. Soc.* **1995**, *142* (5), 1409−1422.

(22) Viswanathan, R.; Hou, G.; Liu, R.; Bare, S. R.; Modica, F.; Mickelson, G.; Segre, C. U.; Leyarovska, N.; Smotkin, E. S. In-Situ XANES of Carbon-Supported Pt-Ru Anode Electrocatalyst for Reformate-Air Polymer Electrolyte Fuel Cells. *J. Phys. Chem. B* **2002**, *106* (13), 3458−3465.

(23) Tibiletti, D.; Amieiro-Fonseca, A.; Burch, R.; Chen, Y.; Fisher, J. M.; Goguet, A.; Hardacre, C.; Hu, P.; Thompsett, D. DFT and in Situ EXAFS Investigation of Gold/Ceria-Zirconia Low-Temperature Water Gas Shift Catalysts: Identification of the Nature of the Active Form of Gold. *J. Phys. Chem. B* **2005**, *109* (47), 22553−22559.

(24) Michailovski, A.; Grunwaldt, J. D.; Baiker, A.; Kiebach, R.; Bensch, W.; Patzke, G. R. Studying the Solvothermal Formation of MoO3 Fibers by Complementary in Situ EXAFS/EDXRD Techniques. *Angew. Chem., Int. Ed.* **2005**, *44* (35), 5643−5647.

(25) Hashmi, A. S. K.; Lothschütz, C.; Ackermann, M.; Doepp, R.; Anantharaman, S.; Marchetti, B.; Bertagnolli, H.; Rominger, F. Gold Catalysis: In Situ EXAFS Study of Homogeneous Oxidative Esterification. *Chem. - Eur. J.* **2010**, *16* (27), 8012−8019.

(26) Zabinsky, S. I.; Rehr, J. J.; Ankudinov, A.; Albers, R. C.; Eller, M. J. Multiple-Scattering Calculations of x-Ray-Absorption Spectra. *Phys. Rev. B: Condens. Matter Mater. Phys.* **1995**, *52* (4), 2995−3009.

(27) Koningsberger, D. C.; Mojet, B. L.; Van Dorssen, G. E.; Ramaker, D. E. XAFS Spectroscopy; Fundamental Principles and Data Analysis. *Top. Catal.* **2000**, *10* (3−4), 143−155.

(28) Enterkin, J. A.; Setthapun, W.; Elam, J. W.; Christensen, S. T.; Rabuffetti, F. A.; Marks, L. D.; Stair, P. C.; Poeppelmeier, K. R.; Marshall, C. L. Propane Oxidation over Pt/SrTiO3 Nanocuboids. *ACS Catal.* **2011**, *1* (6), 629−635.

(29) Tanaka, M.; Tsujimoto, Y.; Miyazaki, T.; Warashina, M.; Wakamatsu, S. Peculiarities of Volatile Hydrocarbon Emissions from Several Types of Vehicles in Japan. *Chemosphere: Global Change Sci.* **2001**, *3* (2), 185−197.

(30) Chang, C. C.; Lo, J. G.; Wang, J. L. Assessment of Reducing Ozone Forming Potential for Vehicles Using Liquefied Petroleum Gas as an Alternative Fuel. *Atmos. Environ.* **2001**, *35* (35), 6201−6211.

(31) Habibpour, V.; Yin, C.; Kwon, G.; Vajda, S.; Palmer, R. E. Catalytic Oxidation of Cyclohexane by Size-Selected Palladium Clusters Pinned on Graphite. *J. Exp. Nanosci.* **2013**, *8* (7−8), 993−1003.

(32) Dummer, N. F.; Bawaked, S.; Hayward, J.; Jenkins, R.; Hutchings, G. J. Oxidative Dehydrogenation of Cyclohexane and Cyclohexene over Supported Gold, Palladium and Gold-Palladium Catalysts. *Catal. Today* **2010**, *154* (1−2), 2−6.

(33) Halder, A.; Ha, M. A.; Zhai, H.; Yang, B.; Pellin, M. J.; Seifert, S.; Alexandrova, A. N.; Vajda, S. Oxidative Dehydrogenation of Cyclohexane by Cu vs Pd Clusters: Selectivity Control by Specific Cluster Dynamics. *ChemCatChem* **2020**, *12* (5), 1307−1315.

(34) Tuysuz, H.; Galilea, J. L.; Schuth, F. Highly Diluted Copper in a Silica Matrix as Active Catalyst for Propylene Oxidation to Acrolein. *Catal. Lett.* **2009**, *131* (1−2), 49−53.

(35) Liu, K.; Chen, Z.; Zou, P.; Wang, Y.; Dai, L. High-Stable CuPd-Cu2O/Ti-Powder Catalyst for Low-Temperature Gas-Phase Selective Oxidation of Alcohols. *Catal. Commun.* **2015**, *67* (3), 54−58.

(36) Negreiros, F. R.; Halder, A.; Yin, C.; Singh, A.; Barcaro, G.; Sementa, L.; Tyo, E. C.; Pellin, M. J.; Bartling, S.; Meiwes-Broer, K. H.; Seifert, S.; Sen, P.; Nigam, S.; Majumder, C.; Fukui, N.; Yasumatsu, H.; Vajda, S.; Fortunelli, A. Bimetallic Ag-Pt Sub-Nanometer Supported Clusters as Highly Efficient and Robust Oxidation Catalysts. *Angew. Chem., Int. Ed.* **2018**, *57* (5), 1209−1213.

(37) Wyrzgol, S. A.; Schafer, S.; Lee, S.; Lee, B.; Vece, M. D.; Li, X.; Seifert, S.; Winans, R. E.; Stutzmann, M.; Lercher, J. A.; Vajda, S. Combined TPRx, in Situ GISAXS and GIXAS Studies of Model Semiconductor-Supported Platinum Catalysts in the Hydrogenation of Ethene. *Phys. Chem. Chem. Phys.* **2010**, *12* (21), 5585−5595.

(38) Timoshenko, J.; Halder, A.; Yang, B.; Seifert, S.; Pellin, M. J.; Vajda, S.; Frenkel, A. I. Subnanometer Substructures in Nano-assemblies Formed from Clusters under a Reactive Atmosphere Revealed Using Machine Learning. *J. Phys. Chem. C* **2018**, *122* (37), 21686−21693.

(39) Liu, Y.; Marcella, N.; Timoshenko, J.; Halder, A.; Yang, B.; Kolipaka, L.; Pellin, M. J.; Seifert, S.; Vajda, S.; Liu, P.; Frenkel, A. I. Mapping XANES Spectra on Structural Descriptors of Copper Oxide Clusters Using Supervised Machine Learning. *J. Chem. Phys.* **2019**, *151* (16), 164201.

(40) Halder, A.; Lenardi, C.; Timoshenko, J.; Mravak, A.; Yang, B.; Kolipaka, L. K.; Piazzoni, C.; Seifert, S.; Bonačić-Koutecký, V.; Frenkel, A. I.; Milani, P.; Vajda, S. CO2Methanation on Cu-Cluster Decorated Zirconia Supports with Different Morphology: A Combined Experimental in Situ GIXANES/GISAXS, Ex-Situ XPS and Theoretical DFT Study. *ACS Catal.* **2021**, *11*, 6210−6224.

(41) Timoshenko, J.; Frenkel, A. I. Inverting" X-Ray Absorption Spectra of Catalysts by Machine Learning in Search for Activity Descriptors. *ACS Catal.* **2019**, *9* (11), 10192−10211.

(42) Marcella, N.; Liu, Y.; Timoshenko, J.; Guan, E.; Luneau, M.; Shirman, T.; Plonka, A. M.; Van Der Hoeven, J. E. S.; Aizenberg, J.; Friend, C. M.; Frenkel, A. I. Neural Network Assisted Analysis of Bimetallic Nanocatalysts Using X-Ray Absorption near Edge Structure Spectroscopy. *Phys. Chem. Chem. Phys.* **2020**, *22* (34), 18902−18910.

(43) Timoshenko, J.; Wrasman, C. J.; Luneau, M.; Shirman, T.; Cargnello, M.; Bare, S. R.; Aizenberg, J.; Friend, C. M.; Frenkel, A. I. Probing Atomic Distributions in Mono- and Bimetallic Nanoparticles by Supervised Machine Learning. *Nano Lett.* **2019**, *19* (1), 520−529.

(44) Elam, J. W.; Sechrist, Z. A.; George, S. M. ZnO/Al2O3 Nanolaminates Fabricated by Atomic Layer Deposition: Growth and Surface Roughness Measurements. *Thin Solid Films* **2002**, *414* (1), 43−55.

(45) Yin, C.; Tyo, E.; Kuchta, K.; Von Issendorff, B.; Vajda, S. Atomically Precise (Catalytic) Particles Synthesized by a Novel Cluster Deposition Instrument. *J. Chem. Phys.* **2014**, *140* (17), 174201.

(46) Lee, S.; Lee, B.; Seifert, S.; Vajda, S.; Winans, R. E. Simultaneous Measurement of X-Ray Small Angle Scattering, Absorption and Reactivity: A Continuous Flow Catalysis Reactor. *Nucl. Instrum. Methods Phys. Res., Sect. A* **2011**, *649* (1), 200−203.

(47) Lei, Y.; Mehmood, F.; Lee, S.; Greeley, J.; Lee, B.; Seifert, S.; Winans, R. E.; Elam, J. W.; Meyer, R. J.; Redfern, P. C.; Teschner, D.; Schlögl, R.; Pellin, M. J.; Curtiss, L. A.; Vajda, S. Increased Silver Activity for Direct Propylene Epoxidation via Subnanometer Size Effects. *Science* **2010**, *328* (5975), 224−228.

(48) Lee, B.; Seifert, S.; Riley, S. J.; Tikhonov, G.; Tomczyk, N. A.; Vajda, S.; Winans, R. E. Anomalous Grazing Incidence Small-Angle x-Ray Scattering Studies of Platinum Nanoparticles Formed by Cluster Deposition. *J. Chem. Phys.* **2005**, *123* (7), 074701.

(49) Keshari, A. K.; Pandey, A. C. Size and Distribution: A Comparison of XRD, SAXS and SANS Study of IIVI Semiconductor Nanocrystals. *J. Nanosci. Nanotechnol.* **2008**, *8*, 1221−1227.

(50) Ilavsky, J.; Jemian, P. R. Irena: Tool Suite for Modeling and Analysis of Small-Angle Scattering. *J. Appl. Crystallogr.* **2009**, *42* (2), 347−353.

(51) Kim, W. B.; Choi, S. H.; Lee, J. S. Quantitative Analysis of Ti-O-Si and Ti-O-Ti Bonds in Ti-Si Binary Oxides by the Linear Combination of XANES. *J. Phys. Chem. B* **2000**, *104* (36), 8670−8678.

(52) Jaumot, J.; Gargallo, R.; De Juan, A.; Tauler, R. A Graphical User-Friendly Interface for MCR-ALS: A New Tool for Multivariate Curve Resolution in MATLAB. *Chemom. Intell. Lab. Syst.* **2005**, *76* (1), 101−110.

(53) Eveillard, F.; Gervillié, C.; Taviot-Guého, C.; Leroux, F.; Guérin, K.; Sougrati, M. T.; Belin, S.; Delbègue, D. Unravelling Lithiation Mechanisms of Iron Trifluoride by: Operando x-Ray Absorption Spectroscopy and Mcr-Als Chemometric Tools. *New J. Chem.* **2020**, *44* (24), 10153−10164.

(54) Rabeah, J.; Briois, V.; Adomeit, S.; La Fontaine, C.; Bentrup, U.; Brückner, A. Multivariate Analysis of Coupled Operando EPR/XANES/EXAFS/UV-Vis/ATR-IR Spectroscopy: A New Dimension for Mechanistic Studies of Catalytic Gas-Liquid Phase Reactions. *Chem. - Eur. J.* **2020**, *26* (33), 7395−7404.

(55) Kurlov, A.; Huang, X.; Deeva, E. B.; Abdala, P. M.; Fedorov, A.; Müller, C. R. Molybdenum Carbide and Oxycarbide from Carbon-Supported MoO3 Nanosheets: Phase Evolution and DRM Catalytic Activity Assessed by TEM and: In Situ XANES/XRD Methods. *Nanoscale* **2020**, *12* (24), 13086−13094.

(56) Saeki, M.; Yomogida, T.; Matsumura, D.; Saito, T.; Nakanishi, R.; Tsuji, T.; Ohba, H. Application of an Augmentation Method to MCR-ALS Analysis for XAFS and Raman Data Matrices in the Structural Change of Isopolymolybdates. *Anal. Sci.* **2020**, *36* (11), 1371−1378.

(57) Ressler, T.; Wong, J.; Roos, J.; Smith, I. L. Quantitative Speciation of Mn-Bearing Particulates Emitted from Autos Burning (Methylcyclopentadienyl) Manganese Tricarbonyl-Added Gasolines Using XANES Spectroscopy. *Environ. Sci. Technol.* **2000**, *34* (6), 950−958.

(58) Jaumot, J.; de Juan, A.; Tauler, R. MCR-ALS GUI 2.0: New Features and Applications. *Chemom. Intell. Lab. Syst.* **2015**, *140*, 1−12.

(59) Windig, W.; Heckler, C. E.; Agblevor, F. A.; Evans, R. J. Self-Modeling Mixture Analysis of Categorized Pyrolysis Mass Spectral Data with the SIMPLISMA Approach. *Chemom. Intell. Lab. Syst.* **1992**, *14* (1−3), 195−207.

(60) Windig, W.; Guilment, J. *Anal. Chem.* **1991**, *63* (4), 1425−1432.

(61) Timoshenko, J.; Lu, D.; Lin, Y.; Frenkel, A. I. Supervised Machine-Learning-Based Determination of Three-Dimensional Structure of Metallic Nanoparticles. *J. Phys. Chem. Lett.* **2017**, *8* (20), 5091−5098.

(62) Rehr, J. J.; Kas, J. J.; Vila, F. D.; Prange, M. P.; Jorissen, K. Parameter-Free Calculations of X-Ray Spectra with FEFF9. *Phys. Chem. Chem. Phys.* **2010**, *12* (21), 5503−5513.

(63) Frenkel, A. I.; Kleifeld, O.; Wasserman, S. R.; Sagi, I. Phase Speciation by Extended X-Ray Absorption Fine Structure Spectroscopy. *J. Chem. Phys.* **2002**, *116* (21), 9449−9456.

(64) Wang, Q.; Hanson, J. C.; Frenkel, A. I. Solving the Structure of Reaction Intermediates by Time-Resolved Synchrotron x-Ray Absorption Spectroscopy. *J. Chem. Phys.* **2008**, *129* (23), 234502.

(65) Khatib, S. J.; Oyama, S. T. Direct Oxidation of Propylene to Propylene Oxide with Molecular Oxygen: A Review. *Catal. Rev.: Sci. Eng.* **2015**, *57* (3), 306−344.

(66) Nijhuis, T. A.; Makkee, M.; Moulijn, J. A.; Weckhuysen, B. M. The Production of Propene Oxide: Catalytic Processes and Recent Developments. *Ind. Eng. Chem. Res.* **2006**, *45* (10), 3447−3459.

(67) Cochran, R. N.; Jubin, J. C.; Liepa, M. A.; Nedwick, R.; Pitchai, R.; Wentzheimer, W. W. Propylene Oxide Productione. U.S. Patent 5 973 171, 1998.

(68) Hayashi, T.; Han, L. B.; Tsubota, S.; Haruta, M. Formation of Propylene Oxide by the Gas-Phase Reaction of Propane and Propene Mixture with Oxygen. *Ind. Eng. Chem. Res.* **1995**, *34* (7), 2298−2304.

(69) Zandkarimi, B.; Sun, G.; Halder, A.; Seifert, S.; Vajda, S.; Sautet, P.; Alexandrova, A. N. Interpreting the Operando XANES of Surface-Supported Subnanometer Clusters: When Fluxionality, Oxidation State, and Size Effect Fight. *J. Phys. Chem. C* **2020**, *124* (18), 10057−10066.